actuators

MDPI

Article

Wavefront Control Strategies for Large Active Thin Shell Primaries with Unimorph Actuators

Kainan Wang [1,2,*,†], Yian Yu [1,†] and André Preumont [3]

[1] School of Remote Sensing and Information Engineering, Wuhan University, Wuhan 430072, China
[2] Hubei Luojia Laboratory, Wuhan 430072, China
[3] Department of Control Engineering and System Analysis, Université Libre de Bruxelles (ULB), CP. 165-55, 50 Av. F.D. Roosevelt, B-1050 Brussels, Belgium
* Correspondence: kainan.wang@whu.edu.cn
† These authors contributed equally to this work.

Abstract: This paper presents various aspects of the wavefront control strategies for an ultra-lightweight composite reflector made of polymers for the large primary of a space telescope, and the shape control is made by a set of patterned unimorph strain actuators attached to the reflector. It starts with an analytical investigation of the mechanical behaviors of a strain-actuated curved shell, resulting in the accurate prediction of typical features, such as the damped wave deformation at the transition between electrodes and the limited morphing amplitude of a "print-through" actuation, which indicates that the curvature-induced rigidity deteriorates the performances of the forming accuracy of the active reflector and the morphing stroke of the actuators. The morphing capabilities are evaluated with both petal-like segmented and monolithic configured reflectors by numerical tests on forming target shapes of Zernike modes with various patternings of electrodes, and the structural dynamics are examined. Finally, a compound control strategy is proposed, which uses a deformable relay mirror to compensate for the residual surface error corrected partially by the active unimorph primary mirror, showing a great relaxation of the shape error budget of the thin-shell primary, especially for on-axis observation.

Keywords: thin-shell reflector; unimorph actuators; petal-like segmentation; compound control strategy; deformable relay mirror

Citation: Wang, K.; Yu, Y.; Preumont, A. Wavefront Control Strategies for Large Active Thin Shell Primaries with Unimorph Actuators. *Actuators* **2023**, *12*, 100. https://doi.org/10.3390/act12030100

Academic Editor: Katsushi Furutani

Received: 29 January 2023
Revised: 21 February 2023
Accepted: 24 February 2023
Published: 24 February 2023

1. Introduction

Future space observation requires large apertures to achieve higher resolution images of celestials in the deep universe. Since the 1980s, an increasing number of ground-based optical telescopes have been built for astronomical imaging, with a primary diameter larger than 8 m; future concepts of extremely large telescopes (ELTs) with $D > 25$ m are also proposed and some are planned to be constructed in the near future [1,2]. However, space telescopes offer an alternative solution rather than ground-based telescopes, to overcome the limitations set by the Earth's atmosphere, enabling a sharp observation without the turbulencing phase variation and allowing for the access of the monitoring to the bands of the electromagnetic spectrum blocked by the atmosphere. However, installing large reflectors in space means more difficulties in technology and budget, from a technical point of view; the first big problem is the transport of massive optical structures to the orbit, because current launchers have tight weight and volume constraints.

The Hubble Space Telescope (HST), launched in 1990 and operated by NASA, was the world's first space-based optical telescope; it has a Ritchey–Chrétien (R-C) configuration with a hyperboloid monolithic 2.4 m primary made of ultra-low-expansion glass (ULE), and a total mass of 826 kg leads to an overall areal density of approximately 180 kg/m^2. The Herschel space infrared telescope was operated by ESA during 2009–2013 and terminated the mission due to a running-out of the coolant; it has a primary mirror of 3.5 m

constructed by brazing 12 petals of Silicon Carbide (SiC) with an areal density of 22 kg/m^2. Unlike the HST, which operates in low Earth orbit (LEO) with a flying height of approximately 570 km and could be repaired by astronauts, the Herschel observatory operated at the more distant Sun–Earth Lagrange point L2 (SE-L2), around 1.5 millions of kilometers from the Earth. The recently launched James Webb Space Telescope (JWST) by NASA uses a lighter design of the reflector of 6.5 m consisting of a honeycomb array with 17 segments: each Beryllium mirror sub-mirror is around 20 kg in mass, and the assembly with actuators weighs about 40 kg leading to an areal density of 20 kg/m^2. The JWST's improvements should also be attributed to the lightweight design of housing structures; the total mass of the JWST is approximately 6500 kg, which is a little more than half the mass of the HST, and this will allow for space delivery to a distant location (e.g., SE-L2). The JWST's primary can be folded in a chord-fold architecture and packaged into the Ariane 5 launch vehicle. Figure 1 illustrates the dimensions of the primaries and the orbital information of those space telescopes [3].

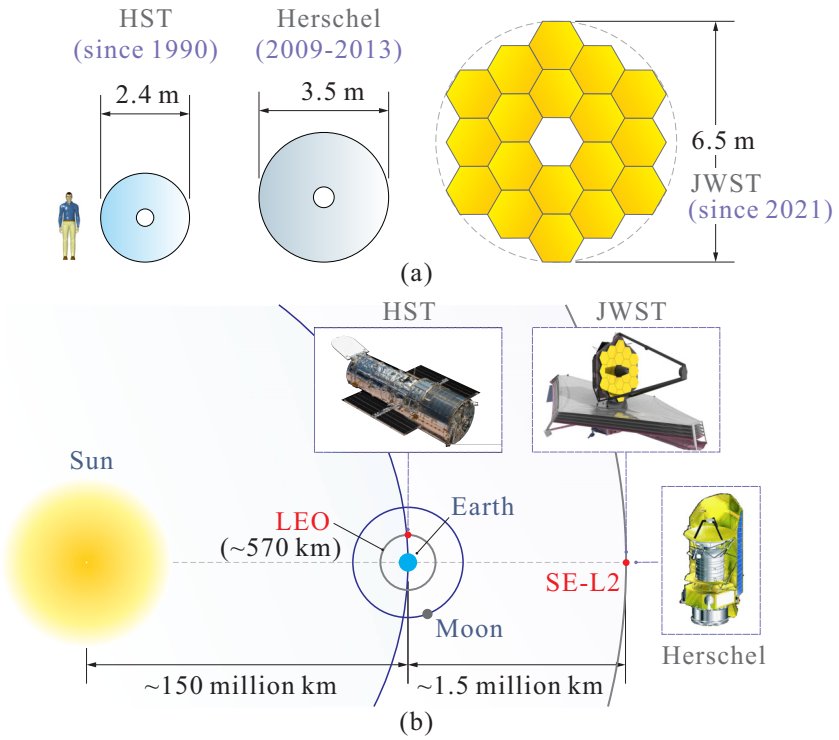

Figure 1. (**a**) Comparisons of the sizes of the primary mirrors of HST, Herschel, and JWST (with a reference height of 1.8 m); (**b**) orbital information of space telescopes.

Different from those mainstream space telescopes using conventional materials for optical application, the novel catalog of reflectors made of polymers has recently attracted the attention of the astronomical community, for their great potential in stowability and areal densities, which offer technical feasibilities for the extremely large platforms of the observatory in space for various wavelengths. Figure 2 gives a view of three broad classes of concepts for polymer reflectors in development: (1) pressure stiffened membranes with inflatable gas maintaining the shape of the reflective surface [4]; (2) membrane antenna reflectors supported by a deployable truss mesh [5]; (3) form stiffened elastic shells with a doubly curved surface [6].

The first two categories of reflectors are usually used as large space antennas with a sufficient surface accuracy for receiving and transmitting microwave signals. The inflatable antenna uses one membrane covered by a reflective coating on the inside as the reflector and another transparent membrane as the canopy. One example was NASA's Inflatable Antenna Experiment (IAE) launched in 1996: the unfolded membrane made of Mylar has

a diameter of $D = 14$ m and is inflated with a tunable internal pressure for adjusting the focal length; the weight of the structure is about 60 kg [7], implying an areal density of 0.39 kg/m^2, and can be stowed in a compact dimension of 2.04 m $\times$ 1.08 m $\times$ 0.5 m. The other concept, the form stiffened thin-shell reflector, uses a layer of polymer to form a delicated shape (to be molded), and the reflector is rolled for stowage and recovered in space by releasing its strain energy; this was firstly proposed and tested on the passive thin-shell reflectors in [8], and other folding and deployment strategies of thin reflectors can be found in [9].

Common polymer materials for space might be PolyEthylene Terephthalate (abbreviated for PET, e.g., Mylar® [4]) or PolyImide (abbreviated for PI, e.g., Kapton® [10]), which are used for film structures such as shields or reflectors. Other potential polymers for space reflectors are still in development, and they call for good surface roughness, a low coefficient of thermal expansion (CTE), and excellent durability. In situ tests for space survivability have been attempted, e.g., a series of spaceflight experiments have been conducted under the framework of the Materials International Space Station Experiment (MISSE) program to test the performance and durability of polymers exposed to the LEO space environment [11].

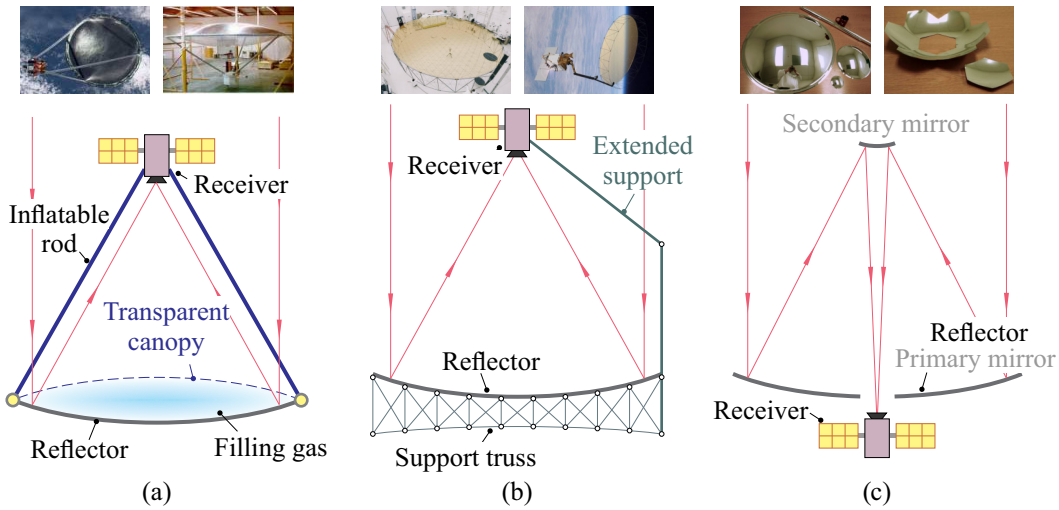

Figure 2. Three broad classes of concepts for polymer reflectors in development: (**a**) pressure stiffened membranes; (**b**) membrane antenna reflectors supported by a deployable truss mesh; (**c**) form stiffened elastic shells of a doubly curved surface. (image credits: L'Garde Inc., Northrop Grumman Corp., Mevicon Inc., and NASA).

The core issue for the applicability of an ultra-light polymer reflector is how to form and maintain a shape with sufficient accuracy, especially with various disturbances in space. The surface accuracy can be measured by the root mean square (RMS) of the deviated shape (error), for which the requirement depends on the observing wavelength; for a space radio antenna, a magnitude of millimeters for the shape RMS error is generally required. However, the error budget for a reflector surface in the optical/infrared range is extremely limited and usually smaller than $\lambda/28$, where λ is the wavelength. Figure 3 presents a literature survey of the shape accuracy with respect to the reflector diameter of existing projects [12,13], showing a trade-off between the size and the precision of a reflective surface under the technological constraint for space and the current development of the polymer for large reflectors is based on inflatable structures only for radio astronomy, where the design focus is on enlarging the collecting area of microwave signals.

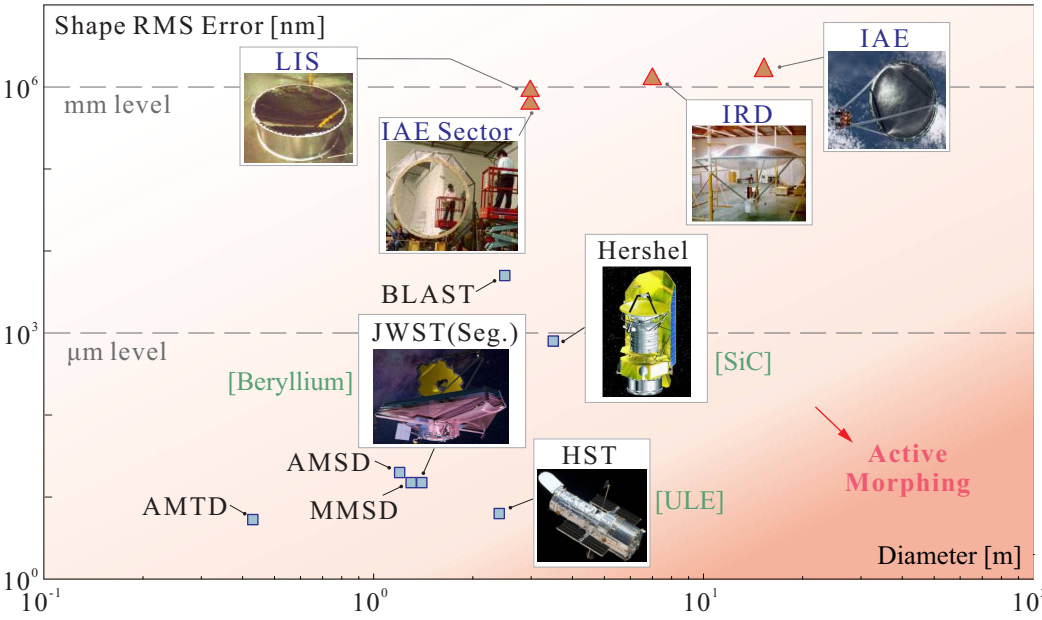

Figure 3. Literature survey of the shape accuracy with respect to the reflector size for various projects (data collected from [12,13], image credits: L'Garde Inc. and NASA).

Unlike most passive reflectors, which maintain their shape by rigidity with a high resistance to space disturbance, the active control of a polymer reflector might be a feasible way for future observation in shorter wavelengths due to a reduction in the structural stiffness. The actuation on the reflector surface can be realized in various methods depending on the configuration and the shape error budget, e.g., by tuning the pressure of filling gas inside inflatable membrane apertures to acquire a proper focal length [4], with electrostatic actuators (acting out of plane) on a mesh antenna [5] or with a set of strain actuators (acting in plane) attached on the back of the reflector in a unimorph manner [14]. Recent studies at Université Libre de Bruxelles (ULB) exhibit possibilities of using a film layer of PolyVinyliDene Fluoride-co-TriFluoroEthylene (PVDF-TrFE) (both piezoelectric and electrostricitive) to actuate the thin-shell mirror, which is curvely molded in a unimorph configuration to correct surface modal errors, and small-scale technology demonstrators have been successfully developed, achieving a shape accuracy that might be used in the infrared range [15,16].

This paper discusses the wavefront control strategies for the formed stiffened thin-shell reflectors with unimorph strain actuators. This paper is organized as follows: Section 2 analyzes the mechanics of strain-actuated curved thin shells, and it starts with the governing equation of an analogical flat plate, and the additional stiffness induced by the curvature is considered, which leads to a fourth-order differential equation controlling the deformation of the surface, with an eigensolution related to the structural parameter, $\sqrt{R_C t}$, where R_C is the radius of curvature and t is the thickness of the reflector. The results can be used to predict the typical features of the morphing behavior such as the damped wave deformation at the electrode transition and the morphing amplitude of a "print-through" actuation, where both deteriorate the performances of the forming accuracy of the active reflector and the morphing stroke of the actuators. Section 3 considers the thin-shell structure for a large-size primary mirror of a telescope, and the softening effect of a petal-like division on the reflector is numerically investigated, with a trade-off pointed out between the larger morphing stroke and increased responses (shape errors) excited by the environmental disturbances. The performances of the forming accuracy are also compared, between the petal-like segmented and monolithic configurations of the reflectors, showing a modal dependency on the capacities of the optical error reduction. Section 4 proposes a compound control strategy for the enhancement of the wavefront correction by supplementing a deformable relay mirror, and an augmentation can be achieved on the error budget of the

shape error for the addition of the complementary correction by the relay mirror, especially for an on-axis observation in space.

2. Mechanics of Strain-Actuated Curved Thin Shells

In this section, the mechanical behavior of a unimorph strain-actuated curved thin shell will be discussed. We begin with a static equilibrium equation of a flat plate governing the vertical motion W of the surface

$$D_B \nabla^4 W = p_z \tag{1}$$

where the flexural rigidity $D_B = Et^3/12(1-\nu^2)$ describes plate bending stiffness: E is the Young's modulus, t is the plate thickness, ν is the Poisson's ratio, and ∇^4 is the double Laplacian operator; p_z represents the distributed load. According to [17], a simple analytical approximation for curved shells suggests that surface curvatures will introduce mid-surface strains (the membrane extension or contraction) and a geometrical strain, which ensures the mid-surface deformation is kinematically compatible, and these can be made by adding two terms to Equation (1)

$$D_B \nabla^4 W + D_M W = p_z + d_z \tag{2}$$

which implies that a curved thin shell behaves similarly to a plate on an elastic foundation in the quasi-static domain. In Equation (2), D_M stands for the foundation modulus and is expressed as

$$D_M = \frac{Et(c_1^2 + 2\nu c_1 c_2 + c_2^2)}{1-\nu^2} \tag{3}$$

where c_1 and c_2 represent curvatures in orthogonal directions; this term can be regarded as the suspension stiffness of connecting an analogical flat plate to the virtual ground. Another additional term, d_z, usually called the "deformation load", is a parasitic load acting when in-plane stretching occurs and can be negligible if the membrane extension is small (we assume $d_z = 0$ in this study). Note that, in this paper, it is not intended to substitute a curved shell by a ground-mounted flat plate with the analogical hypothesis proposed by [17], because they are not fully equivalent with each other; however, it still makes sense to use Equation (2) to predict the main features of a strain-actuated curved shell analytically, since considerable accuracy can be found compared to numerical simulations as shown in the rest of this section.

2.1. Damped Wave Deformation at the Transition between Electrodes

It is a typical feature of strain-actuated curved shells that a wavy deformation occurs at the transition between electrodes excited with different strains; the incremental curvature is concentrated near the edge of the actuator, and gradually vanishes within a distance related to $\sqrt{R_C t}$. This may deteriorate the surface quality after control, with the residual error of high spatial frequencies. The wavy deformation can be predicted analytically: consider a one-dimensional wave solved by Equation (2), with an eigenproblem of

$$\frac{d^4 W}{dx^4} + 4\vartheta^4 W = 0 \tag{4}$$

where the eigenvalue is $\vartheta = \sqrt[4]{D_M/4D_B}$; thus, a general solution for Equation (4) is

$$W(x) = e^{-\vartheta x} \cdot \cos(\vartheta x + \psi) \tag{5}$$

which indicates the wave deformation near the edge of an actuated electrode can be decomposed of a set of harmonic shapes with an exponential decay. We define the *characteristic length* as the reciprocal of the eigenvalue

$$L_c = \frac{1}{\vartheta} = \sqrt[4]{\frac{4D_B}{D_M}} \tag{6}$$

which determines the decay rate e^{-x/L_c} of the damped wave and the wavelength $2\pi L_c$ of the harmonic shape $\cos(x/L_c + \psi)$. This will be illustrated by a numerical example below.

Figure 4a shows a finite element (FE) simulation of a single-curvature (cylinder) shell made of PET ($E = 5.6$ GPa, $\nu = 0.38$, $\rho = 1380$ kg/m^3), deformed by a moment load at one end and fixed at the other. Consider the deformation along the direction of the revolution axis; an illustrated diagram of a one-dimensional estimate of the deformed shape is given on the right side of Figure 4a. For a single-curvature shell ($c_1 = 1/R_C, c_2 = 0$), the characteristic length $L_C = 0.76\sqrt{R_C t}$ according to Equations (3) and (6). Figure 4b compares the deformed shape of the analytical solution for Equation (5) and numerical results (with various radii of curvature R_C and thicknesses t); they are plotted with absolute and normalized values in a logarithmic scale. The length of half a wavelength is verified by the spacing Δx between P_1 and P_2 in Figure 4b, where $\Delta x \approx \pi L_C$. The envelope line $W(x) = e^{-x/L_c}$ is also presented, which defines the influence area of the damped wave on the curved shell.

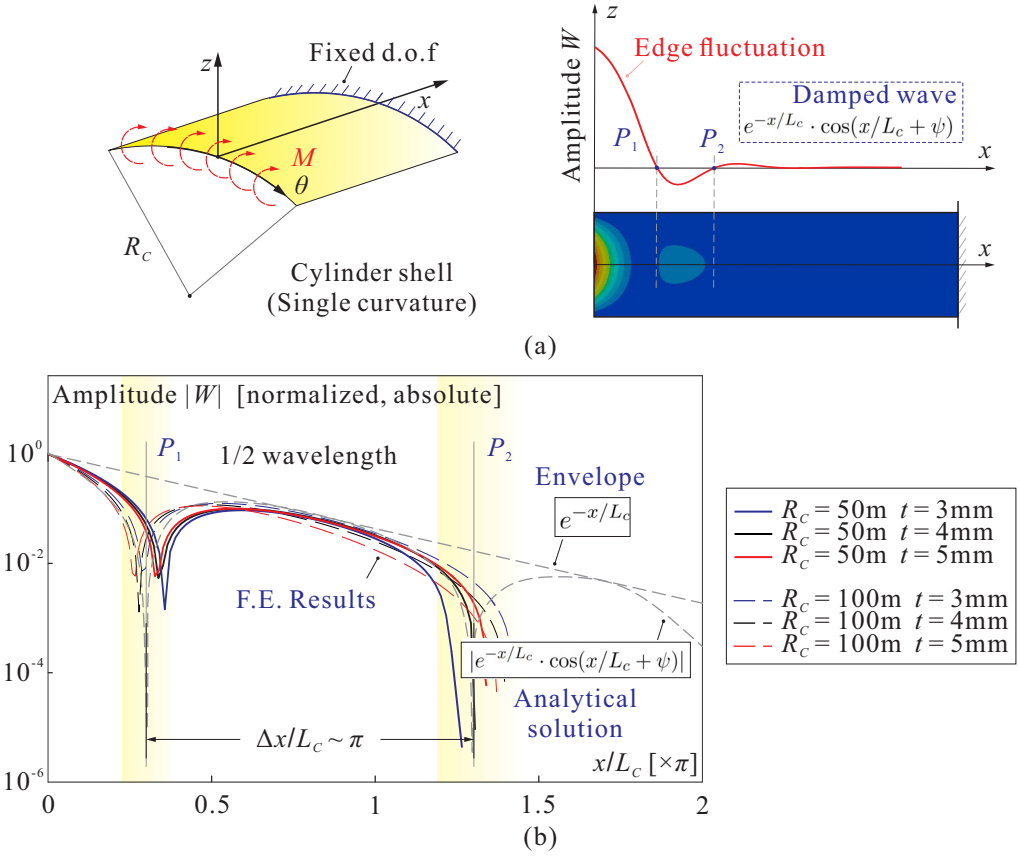

Figure 4. Numerical verification of damped wavy deformation on the edge of a cylinder thin shell with a single curvature ($c_1 = 1/R_C, c_2 = 0$), where the characteristic length $L_C = 0.76\sqrt{R_C t}$ and various radii of curvature R_C and thickness t are tested, showing a good agreement with the analytical solution of Equation (5): (**a**) an illustration of the numerical model of a cylinder shell deformed by a moment load; (**b**) the comparison between the numerical results of the deformation in axial direction and the analytical solution of Equation (5).

Note that, if the shell is doubly curved ($c_1 = c_2 = 1/R_C$), the characteristic length will be $L_C = 0.64\sqrt{R_C t}/\sqrt[4]{1+\nu}$; actually, the effect of ν can always be negligible since $\sqrt[4]{1+\nu} \approx 1$ for most materials with $\nu = 0.0 - 0.5$, unless an auxetic material ($-1 < \nu < 0$) is used for the shell substrate. Therefore, we consider the characteristic length for a spherical shell $L_C = 0.64\sqrt{R_C t}$.

2.2. Equivalent Loads for Unimorph Strain Actuators

In this study, the shell substrate will be covered by a thin layer of linear electroactive film (piezoelectric) and deformed via applying voltages to an array of electrodes. Usually, the unimorph strain actuation on a flat plate can be modeled by a set of equivalent forces consisting of a force normal to the contour of the electrode, which acts in the tangent plane, and a moment acting on the contour of the electrode, e.g., for voltage-driven isotropic piezoelectric film actuators, the force and moment per unit length are, respectively [18],

$$F_E = e_{31} V, \; M_E = e_{31} V t/2 \tag{7}$$

where $e_{31} = d_{31} E_p/(1-\nu_p)$, d_{31} is the in-plane piezoelectric constant, and E_p and ν_p are the Young modulus and the Poisson's ratio of the piezoelectric material. For a spherical shell, a uniform pressure P_E is supplemented to balance the normal component of the force F_E acting on the contour of the electrode

$$P_E = \frac{2F_E}{R_C} \tag{8}$$

which ensures a self-equilibrated actuation since the strain actuation forces are always internal forces [19]. An illustrative diagram of equivalent loads with a central unimorph strain actuator is shown in Figure 5.

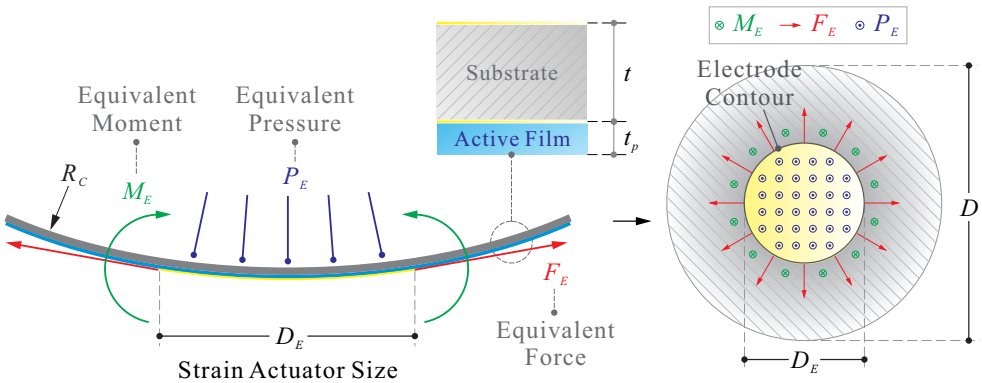

Figure 5. An illustrative diagram of equivalent loads for a unimorph strain actuator acting on a spherical shell.

The shape of a spherical shell excited by the strain actuator is determined by the combination of those different equivalent loads, and the surface morphing can be regarded as linearly superimposed deformation made by different sources. According to Equation (5), there will be an interference of two damped harmonic waves caused by the edge loads from different locations, and thus the morphing behavior is significantly impacted by the separation of the actuator edges (locations of excitations), which is usually defined by the electrode size D_E. Two scenarios need to be specified:

- If the separation of the exciting moments (or other loads acting on the edge) is smaller than 1/4 of the wavelength $2\pi L_C$ (within the monotone interval of a harmonic function) defined in Equation (5), i.e.,

$$D_E \leq \frac{\pi L_C}{2} \simeq \sqrt{R_C t} \tag{9}$$

in which $L_C = 0.64\sqrt{R_C t}$ for a spherical shell, the fluctuated shape near the edge of the actuator will vanish without any ringing profiles.

- If the electrode size is large enough, such that two damped harmonic waves originating near the electrode edge attenuate and have no interaction with each other, the acting area of edge loads (moment or force) will be considered limited. The electrode size D_E in this scenario can approximately be calculated, by assuming the magnitudes of both damped waves are reduced to 1% of their original values when propagating in a distance of $D_E/2$, according to Equation (5), and one obtains $e^{-D_E/2L_C} \leq 0.01$, i.e., $D_E \geq 9.2L_C \simeq 5.9\sqrt{R_C t}$.

Figure 6a shows an evolution of the morphing amplitude excited by a unit voltage, with a change in the dimensionless geometric factor $D_E/\sqrt{R_C t}$. The results are verified by a simulation on a thin ($t = 175$ μm) spherical ($R_C = 1.2$ m) shell with a diameter of $D = 0.4$ m, with a central unimorph actuator of various electrode sizes. In the test, the active layer uses piezoelectric polymer material PVDF-TrFE, with properties of $E_p = 2.5$ GPa, $\nu_p = 0.34$, $\rho_p = 1750\ \mathrm{kg/m^3}$, and $d_{31} = 15$ pC/N.

The first scenario uses a sufficiently small electrode according to Equation (9), i.e., $D_E/\sqrt{R_C t} \leq 1$, leading to a bell-shaped formed surface, with a cross section as shown in Figure 6b (the red curve). Note that, although the morphing amplitude is limited, this shape profile avoids mutual interactions with neighboring actuators, which allows a good fit of the target shape without introducing surface errors of high spatial frequencies. Thus, as a principle, Equation (9) can be considered as the criteria for designing electrodes on a spherical shell.

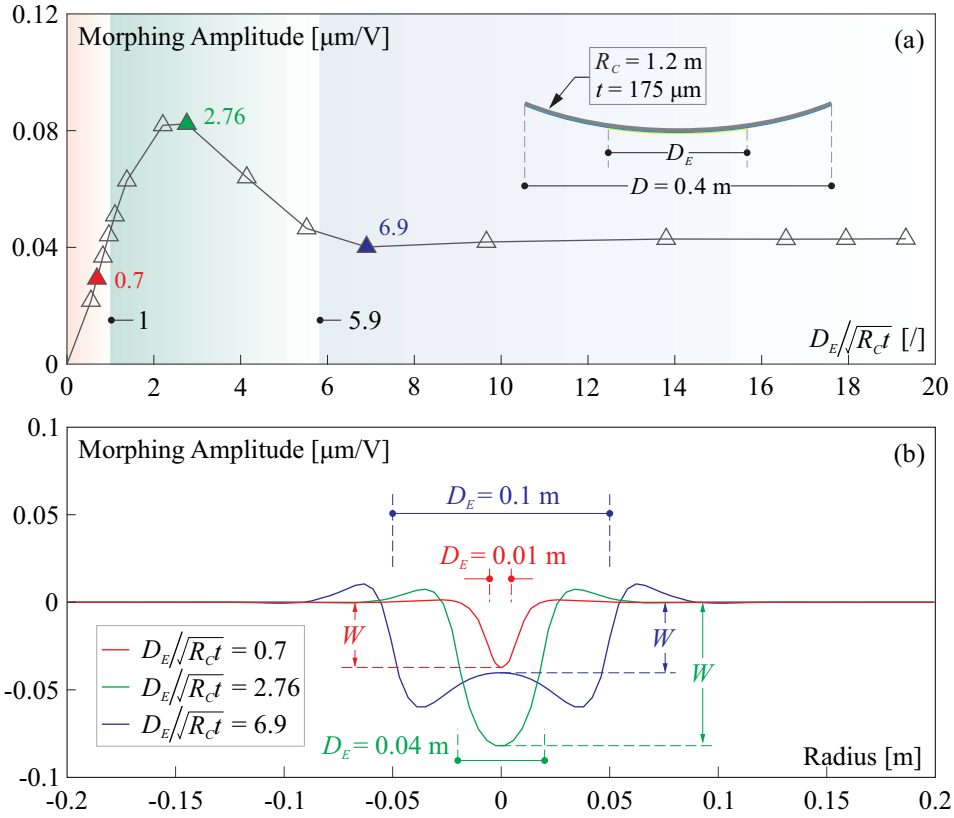

Figure 6. (**a**) The evolution of the morphing amplitude excited by a unit voltage with respect to the dimensionless geometric factor $D_E/\sqrt{R_C t}$, where the amplitude is measured by the relative displacement of the center of the shell structure; (**b**) the cross section shows different morphing behaviors of various $D_E/\sqrt{R_C t}$.

The second scenario considers a larger electrode size with $1 \leq D_E/\sqrt{R_C t} \leq 5.9$. Due to an enhancement of interfering waves, higher actuator strokes can be achieved. However, there will be parasitic errors of unwanted wavy deformation near the electrode edges (see the green curve in Figure 6b). The third scenario uses an electrode size of $D_E > 5.9\sqrt{R_C t}$, where a special phenomenon of "print-through" actuation with the shape of the electrode can be observed. In this scenario, the amplitude of the deformation remains almost constant, and the acting areas of the equivalent moments M_E are well separated; those loads generate exponentially decaying waves, which oscillate near the contour and vanish in the center of the electrode area, as shown in Figure 6b (blue curve). Hence, the amplitude will be controlled by the equivalent pressure P_E in Equation (8), and it is discussed below.

2.3. Amplitude of "Print-Through" Actuation

According to Figure 6b, the "print-through" actuation introduces surface errors of high spatial frequencies with the deformation appearing as the footprint of the electrode, leading to a deteriorating fitting quality of the target shape. This may occur if a large electrode is present or a uniform voltage is used to be applied on a cluster of small neighboring electrodes. The amplitude of the strain actuation when $D_E > 5.9\sqrt{R_C t}$ can be predicted analytically.

Returning to Equation (2), the ratio between the flexural rigidity and foundation modulus $D_B/D_M \propto (R_C t)^2$, in the case of using a very thin and curved shell (with a small value of $R_C t$), the vertical motion due to the mid-surface bending is relatively small, and thus the equation may be rewritten by eliminating the term $D_B \nabla^4 W$, i.e.,

$$D_M W = p_z \tag{10}$$

which describes a single-degree-of-freedom (DoF) system of a pressure-actuated thin shell morphed uniformly within the electrode region. By substituting the distributed load p_z with the equivalent pressure P_E in Equation (8) and combining Equation (7), we obtain

$$W = \frac{P_E}{D_M} = \frac{(1-\nu)E_p d_{31} R_C}{(1-\nu_p)Et} V \tag{11}$$

which gives an approximate calculation of the amplitude of the "print-through" morphing, and this is verified numerically.

Table 1 reports the simulation of the morphing behaviors of a spherical thin shell (diameter: $D = 0.2$ m), with various values of R_C and t tested, and a central unimorph actuator is used with a sufficiently large electrode with a diameter of $D_E > 5.9\sqrt{R_C t}$, and the peripheral of the designed actuator is also far away from the mechanical boundary condition. A comparison of amplitudes computed numerically and analytically is made, which shows a good agreement. It is interesting to observe that, once D_E exceeds the threshold value $5.9\sqrt{R_C t}$, the amplitude can neither be augmented by using a larger electrode diameter D_E, nor changed if a different shell diameter D is employed (compare the case 6 in Table 1 with $D = 0.2$ m and numerical examples in Figure 6 with $D = 0.4$ m); this constraint may pose difficulties for compensating the aberrated shape of a thin-shell structure with a large diameter.

Table 1. Comparisons between numerical and analytical calculations of Equation (11) with a large electrode of $D_E > 5.9\sqrt{R_C t}$.

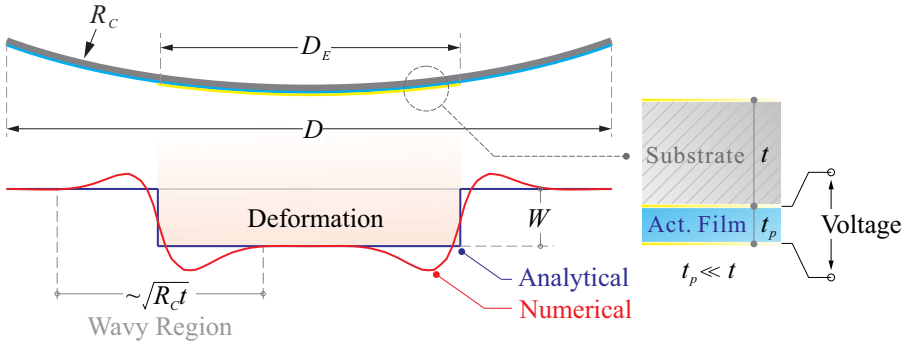

Case	D_E [m]	R_C [m]	t [μm]	$D_E/\sqrt{R_C t}$ [/]	W [μm/V]	
					Numerical	Analytical
1	0.1	2.5	100	6.32	0.1512	0.1573
2	0.1	0.6	100	12.91	0.0373	0.0377
3	0.1	0.8	100	11.18	0.0495	0.0503
4	0.1	1.2	100	9.13	0.0715	0.0755
5	0.07	1.2	100	6.39	0.0719	0.0755
6	0.1	1.2	175	6.90	0.0402	0.0431

3. Unimorph Active Primary Mirror with a Large Diameter

The unimorph curved thin shell will be used for lightweight primary mirrors of space telescopes, with an active morphing capability enabling it to keep a delicated shape, upon the optical design within a certain accuracy. The qualification of an image processed by the telescope optics can be defined by the Strehl ratio S, which is a function of wavefront error w on the image plane

$$S = e^{-4\frac{\pi^2\sigma_w^2}{\lambda^2}} \tag{12}$$

where σ_w is the root mean square (RMS) of the wavefront error; a qualified set of imaging optics calls for a Strehl ratio $S \geq 0.8$, corresponding to a wavefront RMS error of

$$\sigma_w \leq \frac{\lambda}{14} \tag{13}$$

which defines an overall error budget of the optical system. Note that the wavefront variation w introduced by an on-axis reflective surface at the aperture is twice that of the deformed surface W, i.e., $w = -2W$.

Exposed to the harsh space environment, the thin-shell reflector will be excited by various sources, e.g., the thermal and gravitational gradients, and the vibration from supporting frames, resulting in an optical aberration on the image plane of the telescope optics. The disturbance can be also generated internally, e.g., intrinsic thermal loads by the pyroelectric coupling, especially when a large electric field is applied to the thin piezoelectric film. This might be critical under special conditions of heat transfer in space, which can be investigated in future studies, and the theoretical fundamentals can be found in [20]. Other possible factors for producing a surface error on thin-shell reflectors might be the inhomogeneity of stress relaxation or manufacturing errors, causing a quasi-static deviation from their perfect form.

It is difficult to make an accurate prediction for the shape aberration disturbed by those environmental excitations with temporal and spatial uncertainties. Therefore, a feedback control strategy of the wavefront is employed to compensate for the shape error in real-time. This control loop requires a wavefront sensor, which feeds a measurement of the residual

wavefront to the controller, for computing a voltage pattern to the actuator array; in this study, a perfect wavefront sensing is assumed.

The aberrations of the optical wavefront w on the pupil with a diameter of D can be decomposed as a set of orthogonal and normalized functions $Z_i(\rho, \theta)$ defined on a unit circle in polar coordinates called the Zernike modes (or Zernike polynomials)

$$w(D\rho/2, \theta) = \sum c_i Z_i(\rho, \theta) \tag{14}$$

where c_i is the coefficient for the mode i, and $\sigma_w^2 = \sum |c_i|^2$. The analytical expressions of the low-order Zernike polynomials are given in Appendix A. Typical modes depicting the on-axis abberations are Defocus (Z4) and Spherical Abberation (Z11), and the modes of Astigmatism (Z5/6) and Coma (Z7/8) are common off-axis abberations. In the following study, we will also use Zernike modes as modal basis functions to fit the shape deviation of the surface in the telescope optics.

In this section, we will evaluate the morphing capabilities of forming certain Zernike modes for an active primary mirror with a diameter of the order of meters, which is unimorphly actuated by a large array of electrodes; this thin-shell reflector is used as a prime wavefront corrector at the telescope aperture, and both actuator strokes and the surface fitting error will be discussed for different configurations of the reflectors.

3.1. Evaluation on Morphing Capabilities

Two aspects needs to be concerned when assessing the morphing capabilities for a unimorph curved thin shell: (1) the forming accuracy of the active surface, with a measure of the wavefront RMS error σ_w for forming a target shape with a unit amplitude, i.e., peak to valley (PV), denoted by $\delta = \sigma_w/\text{PV}$; (2) the morphing stroke, the amplitude of deformed surface (best fit of the forming target) with respect to the voltage range, denoted by $\text{PV}/\Delta V$. Note that, according to previous studies and the analysis in Section 2, strain-actuated curved shells show a great weakness in both aspects, in a comparison with analogical flat plates. Some attempts have been made to offset those disadvantages; the first one is to reduce the size of the electrodes following Equation (9), resulting in a significant increase in the number of electrodes N, which can be estimated by

$$N \simeq (\frac{D}{D_E})^2 \geq \frac{D^2}{R_C t} = \frac{D}{2(f/\sharp)t} \tag{15}$$

where $f/\sharp = R_C/2D$ is the f-number of the reflector. Controlling with such a large number of actuators means a good fitting of the target shape; however, the morphing amplitude is still limited according to Figure 6a with a small size of electrode. Moreover, a complex control algorithm should be developed to make an accurate inverse of the Jacobian matrix with large dimensions.

The second attempt is to use a petal-like segmented configuration of the reflector instead of a monolithic one, aiming at reducing the hoop stiffness induced by the curvature; this will generally increase the morphing stroke of the actuator array with a (compromised) reasonable number of actuators. The present work is a follow-up to [19,21], and a comparative analysis will be conducted as follows, on the morphing capabilities of forming Zernike modes between the petal-like segmented and monolithic thin curved mirrors.

Figure 7 shows numerical tests for a thin-shell primary mirror used in an infrared telescope: the shell has layers with the passive coated PET substrate and the piezoelectric PVDF-TrFE membrane with in-between electrodes, the gold coating layer is used for increasing the infrared reflectance, and the patterned electrodes are arranged in a keystone layout with the radial order n_R and the azimuth order n_{AZ}. Figure 7a gives the geometric information for the curved shell structure: the primary mirror has a clear aperture of

$D = 1$ m and a central obstruction ratio of 10% (i.e., $D_H = 0.1$ m); for non-paraxial optics (usually for large apertures), the mirror shape with active control can be defined by

$$S_m = \frac{r^2}{R_C + \sqrt{R_C^2 - (1+K)r^2}} + W \tag{16}$$

It has two parts, and the first one, $r^2/(R_C + \sqrt{R_C^2 - (1+K)r^2})$, is the nominal shape, where r is the coordinate of the radial distance, K is the conic constant, and a departure from the sphere ($K = 0$) is often adopted for the primary mirror at the entrance pupil. The value of K for optical surfaces controls the performances of telescopes, e.g., the Cassegrain telescope uses a concave paraboloid primary ($K = -1$) with a convex hyperboloid secondary ($K < -1$) to eliminate the on-axis spherical aberration (Z11); other designs for a reflective telescope can be found in [22]. In this test, a paraboloid reflector ($K = -1$) with $R_C = 2.5$ m is used. The second part, W, is the deviated shape with respect to the nominal one, and might be expressed as $W = e - Jv$, where e is the shape error (compensated target) and Jv is the active formed shape, J is the Jacobian matrix mapping actuator inputs (voltages) to the morphing surface, and v is the vector of the applied voltages.

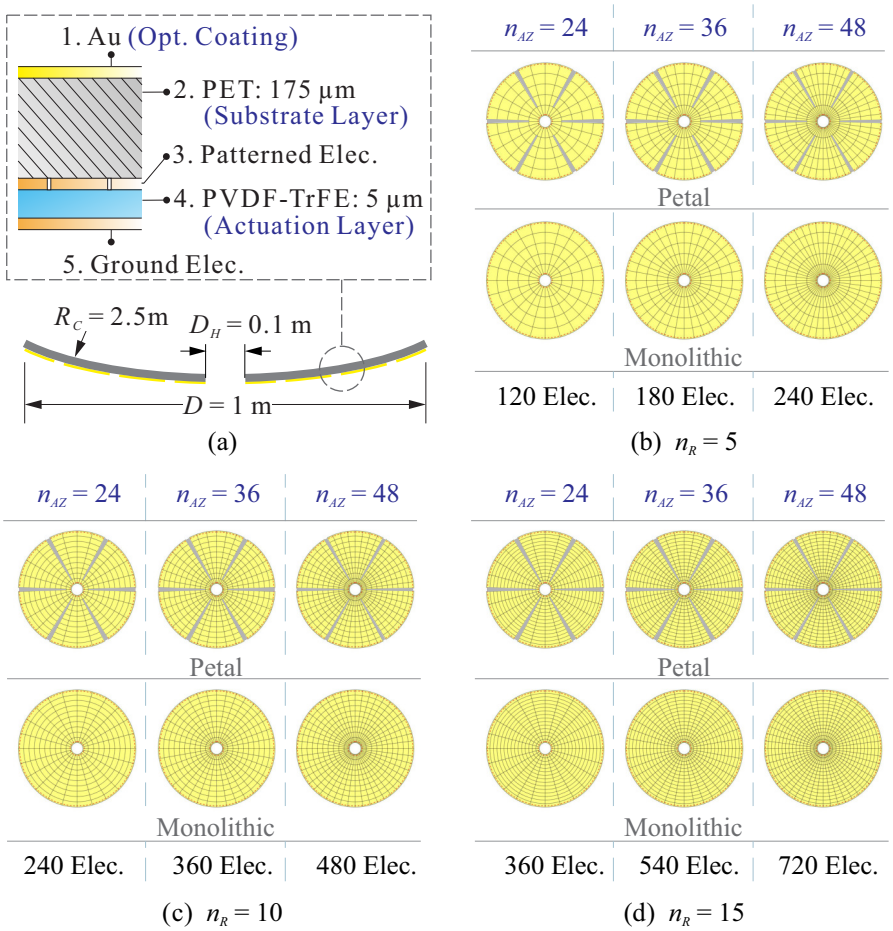

Figure 7. Numerical models for the configuration study of morphing capabilities: (**a**) the structural parameters of the tested composite primary reflector; (**b**–**d**) electrode patterns of numerical examples with radial orders of $n_R = 5$, 10, and 15 and azimuthal orders of $n_{AZ} = 12$, 24, and 36. The performances of both monolithic (full) and petal-like (division order: $m = 6$) configurations are examined.

The voltages can be computed using a least-squares (LS) reconstruction to minimize $\|e - Jv\|_2$, and thus the applied voltages and the residual wavefront error are, respectively,

$$v = (J^T J)^{-1} J^T e,\ w = -2W = 2[J(J^T J)^{-1} J^T - I]e. \tag{17}$$

Figure 7b–d show simulated cases with the layers of various patterned electrodes, and several values of n_R (5/10/15) and n_{AZ} (12/24/36) are tested. In addition, both petal-like segmented (with a division of m = 6) and monolithic configurations are examined.

Figure 8 plots the simulated performance of active shells on forming some low-order Zernike modes; the wavefront RMS error σ_w and voltage range ΔV are computed via Equation (17), where the compensated target is substituted by $e = Z_i$ for the i-th Zernike mode. The results are presented in a form of plotmatrix, in which each subplot shows the relationships of the morphing amplitudes in a given voltage (PV/ΔV) versus the normalized forming accuracies ($\delta = \sigma_w$/PV) for various electrode patterns. According to those results, significantly larger amplitudes of the deformation can be found for petal configurations, for generating a target shape where the curvatures in orthogonal directions have the same signs (Defocus Z4, Coma Z7, and Spherical Aberration Z11). The active reflector with a petal-like division presents excellent performance for the surface error reduction for forming Defocus Z4, and this can be impacted by the radial order n_R of the electrode pattern; when the targets are Coma Z7 and Spherical Aberration Z11, even a slight degradation can be observed (for Spherical Aberration Z11) compared to monolithic (full) configured reflectors.

In contrast, the monolithic configuration shows better performance in both morphing strokes and surface precision when forming a target shape; where the curvatures in orthogonal directions have opposite signs that are wavy on the edge (Astigmatism Z5 and Trefoil Z10), the performance will be degraded for the petal configuration but still within an acceptable range due to the inherently good performance of the full-coverage configuration.

In general, the performance for wavefront error reduction can be improved by a finer patterning of the electrode array (i.e., by using large values of n_{AZ} and n_R for the keystone layout); this applies for most cases in Figure 8, except that the performance of the monolithic configuration is insensitive to the radial order n_R when forming target shapes with periodically fluctuated edges (Astigmatism Z5 and Trefoil Z10) or axisymmetric shapes (e.g., Defocus Z4 and Spherical Aberration Z11). On the other side, the increased number of electrodes deteriorates the Jacobian matrix conditioning, leading to a larger consumption of the applied voltages. Table 2 lists the results of the modal reconstruction for 10 μm amplitude shapes of Defocus Z4 and Astigmatism Z5; the condition number of J is computed by the ratio between the maximum and minimum singular values of the matrix, and this increases with the electrode number. In addition, a reference case with a monolithic configured reflector is also reported, and the electrode number $N = n_R n_{AZ} = 2250$ is chosen to be close to the approximate value based on Equation (15); thus, a good performance can be expected for the wavefront error reduction. Note that petal-configured active reflectors require much fewer electrodes and exhibit better performances in achieving larger actuation strokes.

Figure 9 presents the performances for the active wavefront control of the unimorph shell with respect to the petal number m with a target shape of 10 μm. Finer divisions of sub-reflectors result in better performances for morphing strokes (less voltage required) and surface accuracies when forming the target shapes of Defocus Z4 and Spherical Aberration Z11, showing a relaxing of the error budget for those on-axis aberrations. Similar to the above results, the residual error becomes large (within an acceptable range) with the number of petals for the target shapes with periodically fluctuated edges. Various options for the petal divisions allow for a potential optimal design for stowing the reflector during the launch.

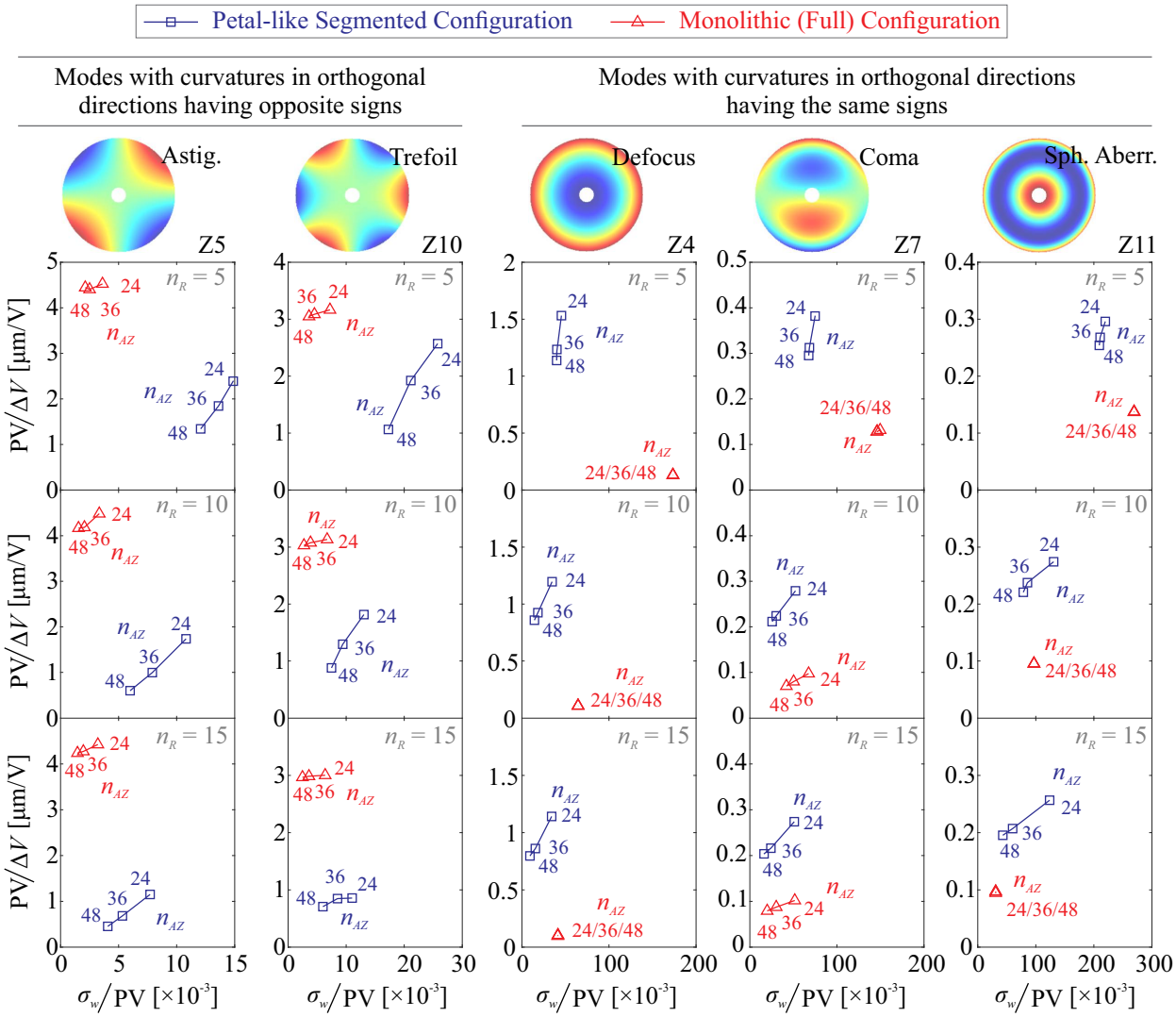

Figure 8. Simulated results of forming low-order Zernike modes with the layer of various reflector configurations and patterned electrodes shown in Figure 7, with both the wavefront RMS error σ_w and voltage range ΔV computed. According to those results, significantly larger amplitudes of the deformation can be found for petal configurations, for generating a target shape where the curvatures in orthogonal directions have the same signs; the monolithic configuration shows better performance in both morphing strokes and surface precision when forming a target shape where the curvatures in orthogonal directions have opposite signs that are wavy on the edge.

Table 2. Numerical results of controlled surface precision (wavefront RMS error) of forming 10 μm amplitude Zernike modes of primary optical aberrations.

n_R	n_{AZ}	Config.	Electrode Number	Condition Number	Defocus Z4		Astigmatism Z5	
					σ_w [nm]	ΔV [V]	σ_w [nm]	ΔV [V]
15	36	Petal-6	540	4211.7	154.36	11.61	53.29	14.65
15	48	Petal-6	720	6701.2	92.16	12.55	40.65	22.04
20	48	Petal-6	960	8216.9	85.93	13.13	28.09	13.35
25	90	Full	2250	132574.2	124.13	722.49	3.76	2.81

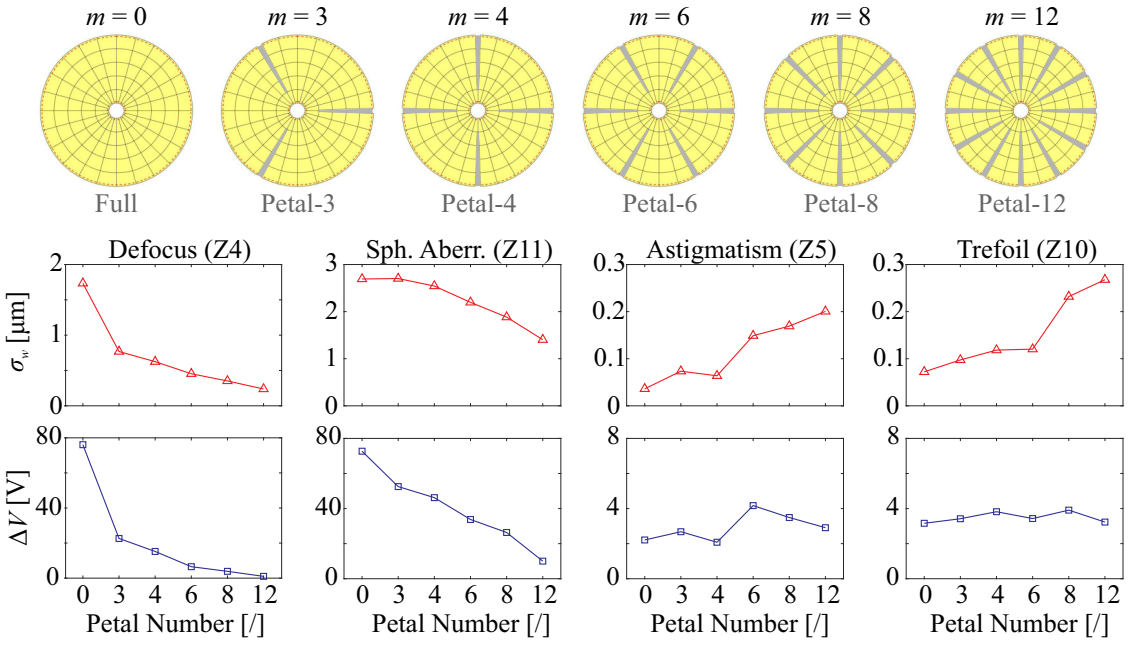

Figure 9. Performances of active surface control (the wavefront RMS error σ_w and the voltage range ΔV) with different numbers m of petal segmentation. The electrodes are arranged with a keystone pattern of $n_R = 5$ and $n_{AZ} = 24$, and the amplitude of the target shape is PV = 10 μm.

3.2. Structural Dynamics

Usually, there is a trade-off between structural rigidity and morphing capabilities for an active space reflector. Rigid structures always have a higher resistance to complex disturbances in space, leading to a restrained magnitude of shape aberrations. This is advantageous for maintaining the reflector in its original shape. However, the morphing capability of a deformable reflector can be significantly deteriorated by a rigid design, especially for the actuator stroke. The responses (shape errors) of a thin-shell reflector by the excitations in space can be assessed by the dynamic characteristics of the structure, where an important measure for this is the resonant frequency ω (in rad). In general, the quasi-static deformation W of a structure can be roughly associated with ω by $W \propto \omega^{-2}$ [23]. For a thin plate structure, the resonant frequency ω_P can be predicted theoretically by

$$\omega_P = \alpha(tD^{-2})\sqrt{\frac{E}{\rho(1-\nu^2)}} \tag{18}$$

where the structural dynamics are determined by the geometric factors tD^{-2} and material factors $E/\rho(1-\nu^2)$, and α is a constant controlled by the boundary condition. Using the models of circular PET flat plates (similar to the cases in Figure 7), which are isostatically supported at the inner edge, a fitted value of $\alpha = 3.13$ can be obtained, with a range for the geometric parameters of $D = 0.5 - 1.5$ m and $t = 100 - 250$ μm. The dynamic behaviors become complicated if a large shell structure is curved, and a literature review shows an establishment of conditionally valid formulae for evaluating the natural frequency ω_S for spherical shells by their analogical flat plates [24]. In this study, we develop a phenomenological model for ω_S by rewriting Equation (18) and using exponential functions on the geometric factors of the curved shell

$$\omega_S = \beta(R_c^a t^b D^c)\sqrt{\frac{E}{\rho(1-\nu^2)}} \tag{19}$$

where the fitted values of $\beta = 1.433$, $a = -0.16$, $b = 0.8$, and $c = -2.08$ can be obtained with a wide range of $R_C = 0.4 - 100$ m (a total of 167 random numerical cases are tested).

The exponent $a < 0$ (for R_C) shows the structural stiffness increases with the curvature of the reflector. Note that $a = -1$ can be used for very curved shells when the curvature-induced stiffness dominates the structural dynamics [8]. The resonant frequencies are also influenced by other factors, such as membrane tensioning and large initial shape aberrations, which are numerically verified in [25].

Figure 10 illustrates the softening effect of the petal segmentation on a curved thin-shell reflector. The numerical examples in Figure 7 are tested, and the resonant frequency (plotted in Hz) decreases with the petal number because the division of the reflector reduces the hoop stiffness. Therefore, larger responses to the disturbances might be present for the petal configured reflectors, resulting in a larger shape error to be compensated by those strain actuators.

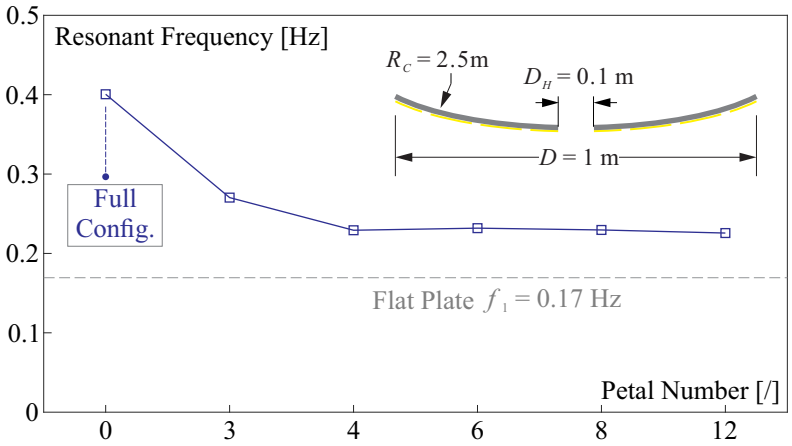

Figure 10. Resonant frequencies of a curved thin shell with respect to the petal numbers.

4. Compound Control with a Deformable Relay Mirror

The active thin-shell reflector acts as a self-corrector maintaining the designed shape and compensates wavefront aberrations at the telescope aperture; a shape error budget can be defined for the primary mirror (the entrance pupil), which causes the wavefront error on the image plane in such a way that

$$\sqrt{\sum_{i=1}^{N} \gamma_i^2} \leq \eta \frac{\lambda}{14} \tag{20}$$

where γ_i is the RMS error budget of the residual wavefront for the Zernike mode i ($i = 1 - N$), η represents the weighting factor of the error allocated to the primary mirror, with the rest, $\sqrt{1-\eta^2}$ of the overall budget $\lambda/14$, for other optical components in the system. In another sense, we can accordingly define a modal shape error budget for the amplitude A_i, by using $A_i = \gamma_i/\delta_i$, where δ_i is the normalized forming accuracy of the mode i as computed in Figure 8; a large value of δ_i indicates insufficient capabilities for forming the mode, leading to a limitation on the achievable amplitude (small value of A_i) for the modal reconstruction. In this section, we propose a compound control strategy using a deformable relay mirror to compensate the residual wavefront error, which has been corrected partially by the active unimorph primary mirror, and the goal of the additional wavefront corrector is to relax the stringent budget on A_i.

This study is based on a classical R-C design of space telescope as shown in Figure 11: the telescope optics consist of a hyperboloid concave primary mirror and a hyperboloid convex secondary mirror, and this configuration eliminates passively both typical optical errors of on-axis Spherical Aberration Z11 and off-axis Coma Z7/8, enabling a wide field for observation and is widely used for astronomical telescopes. The active primary mirror uses the structural parameters of the unimorph thin shell investigated in Section 3 with a conic constant of $K = -1.01$ (very close to the paraboloid mirror). The telescope is designed

with a full FoV of 9.6 arcmin and an overall f-number of 9. A deformable relay mirror is utilized to fold the optical path, and the deformation W_D is actively controllable to abate the optical error made by the residual shape error W of the primary. Two parameters determine the layout of this mirror: the folding angle θ and the distance L to the secondary mirror, which influence the compactness of the space telescope structure.

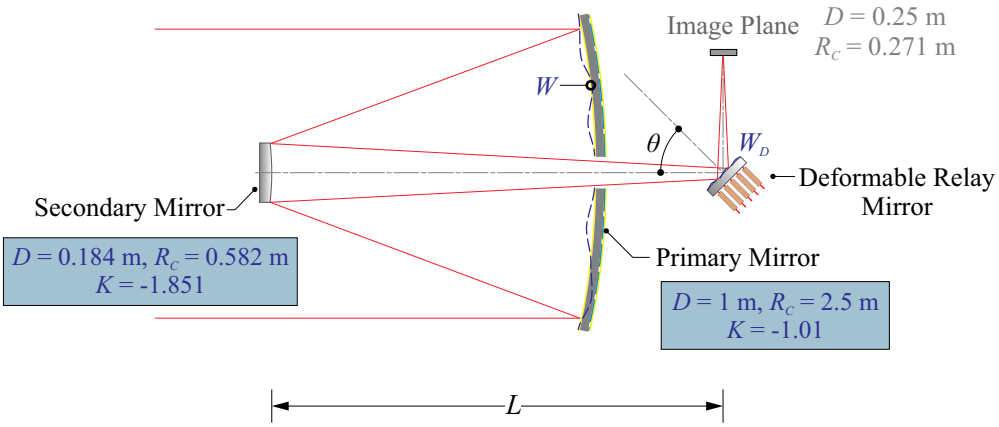

Figure 11. A Ritchey–Chrétien (R-C) design of space telescope: a relay mirror is added to fold the optical path; both primary and relay mirrors are deformable ($L = 1.4$ m, $\theta = 45°$).

The shape deviation of the primary mirror (thin-shell reflector) is set to be $W = \sum a_i Z_i$ at the entrance pupil, and the deformable relay mirror with a shape of $W_D = \sum b_j Z_j$ is used to compensate the wavefront error of the aberrated primary. Both surfaces are decomposed into Zernike modes with vectors of coefficients a and b, respectively. A mapping matrix T exists, which associates two deviated surfaces in the telescope system for eliminating the optical errors on the image plane. The vector b for the required shape W_D is computed by

$$b = Ta \tag{21}$$

in which the matrix T is obtained by utilizing the ray tracing technique, with an inverse optimization process on minimizing the central moment of spots diagram on the optical terminal. Note that this method applies for other sources of optical errors, e.g., the shape error of the secondary mirror or the misalignment within optical surfaces. Usually, the entries of T are the functions of the folding angle θ and the FoV. Figure 12 gives a view of the elements in T, where the mapping orders for a_i and b_j are $i = 4 - 15$ and $j = 4 - 21$, respectively, the modes of Piston (Z1) and Tilt (Z2/3) are not involved because they do not affect the image quality, and $L = 1.4$ m is a constant in this example.

According to Figure 12a,b, the error compensation for on-axis observation shows a good diagonal decoupling between corresponding modes, and the magnitudes of the matrix entries are reduced when a small $\theta = 20°$ is present, due to a change in the elliptical footprint of the incoming light path and the reflection projections. If the FoV is large (see the full FoV for Figure 12c,d), the diagonality of T is broken down due to a complex combination of modes for off-axis monitoring, which is always required, and the relay mirror has a weakly optical conjugation to the primary reflector at the entrance pupil.

The design requirements for the deformable relay mirror are also influenced by the distance L between optical surfaces. Figure 13 shows changes in the required pupil diameter and forming amplitude with respect to L, and both on-axis and full FoV are considered, with a folding angle of $\theta = 20°$. The clear pupil defines the minimal mechanical diameter of a deformable mirror, and a geometric calculation shows a decreasing size of the mirror with L, leading to a (limited) small actuator pitch for the deformable relay. When a wide FoV is used, the mirror size should be increased for off-axis modal correction. Figure 13b gives numerical results for the relative amplitude of compensating the corresponding mode when a shape error of Astigmatism Z5 on the primary mirror is present; for a full FoV

observation, a significant large actuation stroke is required for a large L, and the relative amplitude is almost constant for the on-axis ray tracing. Note that a large value of L poses technical difficulties for the design of the deformable mirror, because a small size is needed with a large morphing stroke.

We assume the deformable mirror performs as a perfect Zernike mode modulator within its own circular pupil, which is technically feasible for some current commercial products [26]. Numerical tests are conducted on the wavefront error reduction on the image plane (collocated with the terminal of the wavefront sensor) as shown in Figure 11, and the error is caused by a shape deviation of the primary mirror with a Zernike mode of unit amplitude. The correction can be made by the active primary mirror using Equation (17) or by deformable relay mirror by a mode mapping optimization using Equation (21). The simulated results for each Zernike mode are plotted in Figure 14, and they show that a significant reduction can be made by the deformable mirror for the on-axis wavefront correction, especially for low-order modes ($i < 10$). With a wider FoV, however, the performance for wavefront compensation becomes limited, with a weighted summation of the residuals over a full range of the fields and this is because the required shape projected on the pupil of the deformable mirror varies with the fields when the error occurs at the entrance pupil; usually, a direct correction on the primary mirror gives better performances than morphing the supplemented optical components.

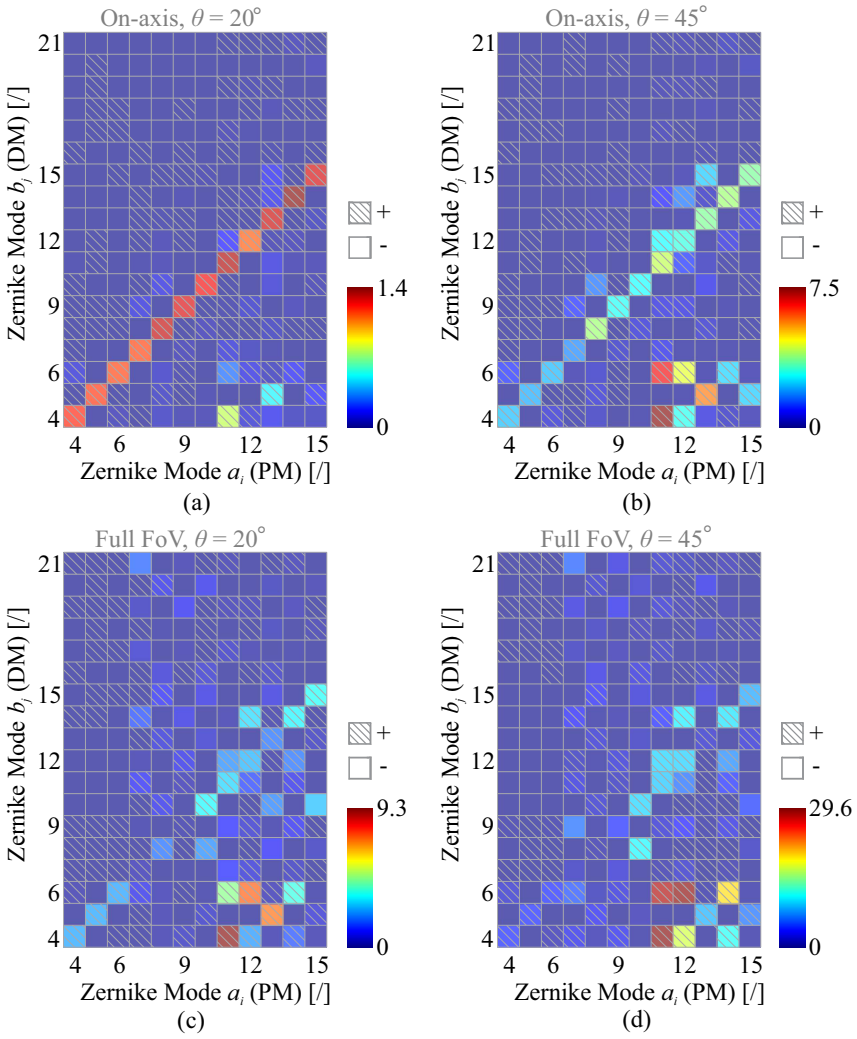

Figure 12. Elements in the matrix T in an absolute value, where the mapping orders for a_i and b_j are $i = 4 - 15$ and $j = 4 - 21$, respectively. Four configurations are plotted: (**a**) on-axis, $\theta = 20°$; (**b**) on-axis, $\theta = 45°$; (**c**) full FoV, $\theta = 20°$; (**d**) full FoV, $\theta = 45°$.

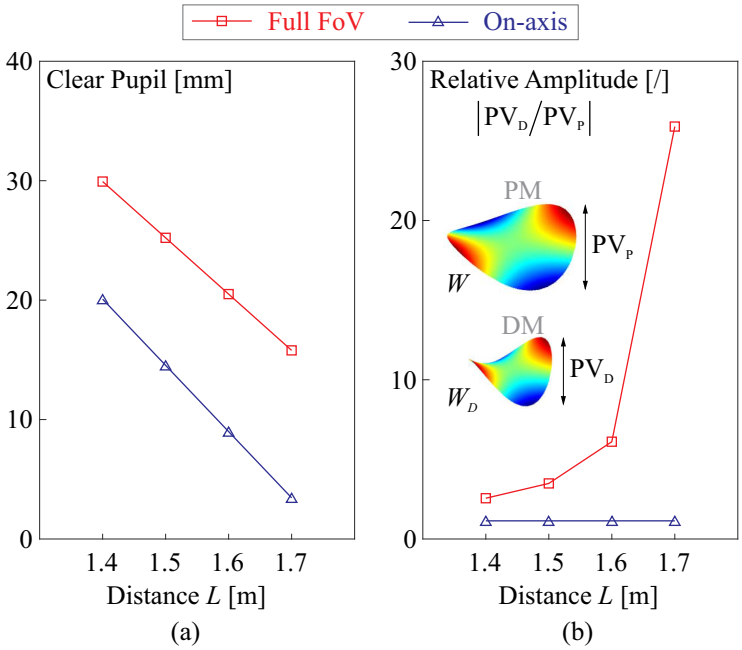

Figure 13. (**a**) Required pupil diameter and (**b**) forming amplitude (for Astigmatism Z5) with respect to L; both on-axis and full FoV are considered, with a folding angle of $\theta = 20°$.

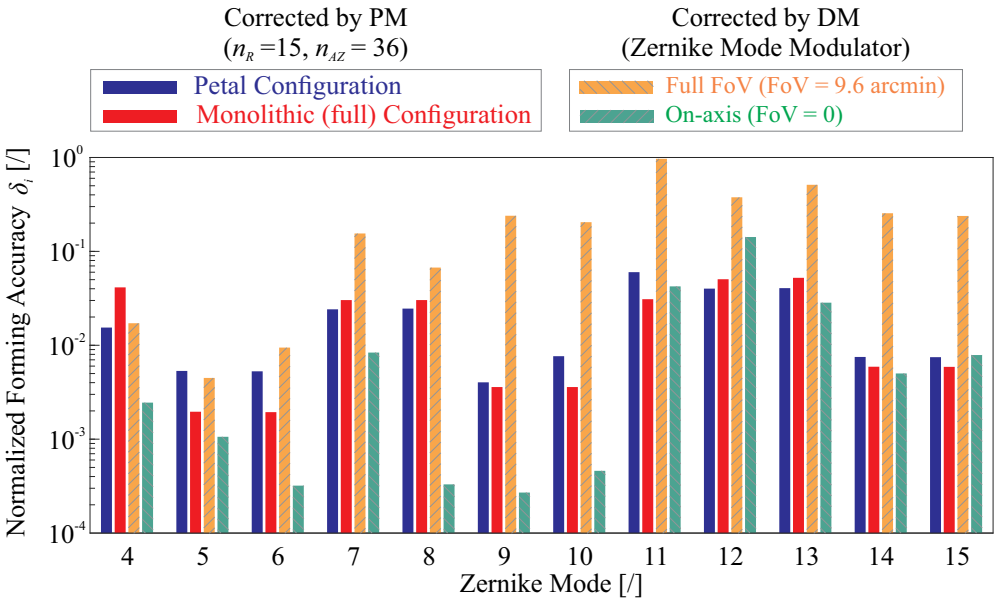

Figure 14. Evaluation of capabilities of wavefront correction for active primary and relay mirrors: the primary mirror has a keystone electrode pattern with $n_R = 15$ and $n_{AZ} = 36$ with both petal-like and monolithic configurations plotted; the effect of FoV on the optical error compensation with the deformable mirror is considered.

The deformable relay mirror enables a complementary correction of the wavefront error caused by the thin-shell primary mirror, which can be easily excited with a large deformation. Hence, we may allocate the amplitude of the aberrated shape of a primary surface (in the Zernike mode i) A_i into A_i^P and A_i^D (i.e., $A_i = A_i^P + A_i^D$), allocating them, respectively, to the unimorph thin-shell reflector itself and the deformable relay mirror for error elimination on the image plane of the telescope optics. This leads to an optimiza-

tion problem solving the maximum possible amplitude A_i^{max} of the error budget of the primary mirror.

$$max(A_i^P + A_i^D) \quad subject\ to\ \sqrt{(A_i^P\delta_i)^2 + (A_i^D\delta_i^D)^2} \leq \gamma_i \tag{22}$$

where δ_i^D is the normalized forming accuracy for the mode i of the deformable mirror as computed in Figure 14 and γ_i of the RMS error budget defined in Equation (20). The mathematical solutions for Equation (22) are

$$A_i^P = \frac{\delta_i^D}{\sqrt{(\delta_i)^4 + (\delta_i^D\delta_i)^2}}\gamma_i, \quad A_i^D = \frac{\delta_i}{\sqrt{(\delta_i^D)^4 + (\delta_i^D\delta_i)^2}}\gamma_i \tag{23}$$

Figure 15 shows the maximum allowed values of the amplitudes for the shape error in Zernike modes (with a unit of wavelength λ), and the computation uses Equation (23) with the RMS error budget γ_i equally distributed for the modes $i = 4 - 15$ in Equation (13) (assuming $\eta = 0.5$); a more delicated budget design on γ_i can be made if a reduction in certain modes is needed. According to Figure 15, for an on-axis observation, the error budget in amplitude for a thin-shell reflector can be increased by approximately an order of magnitude, by supplementing a deformable mirror into the optical chain; this benefit can be extended for a narrow field of view monitoring on a distant object. However, this benefit might be lost for a wider FoV, with a dominant capacity of correcting wavefront errors by the primary mirror over a wide range of field. Note that a weighting factor can be added for the allocated amplitude A_i^D of the deformable relay mirror, if the energy consumption for the actuation is taken into account.

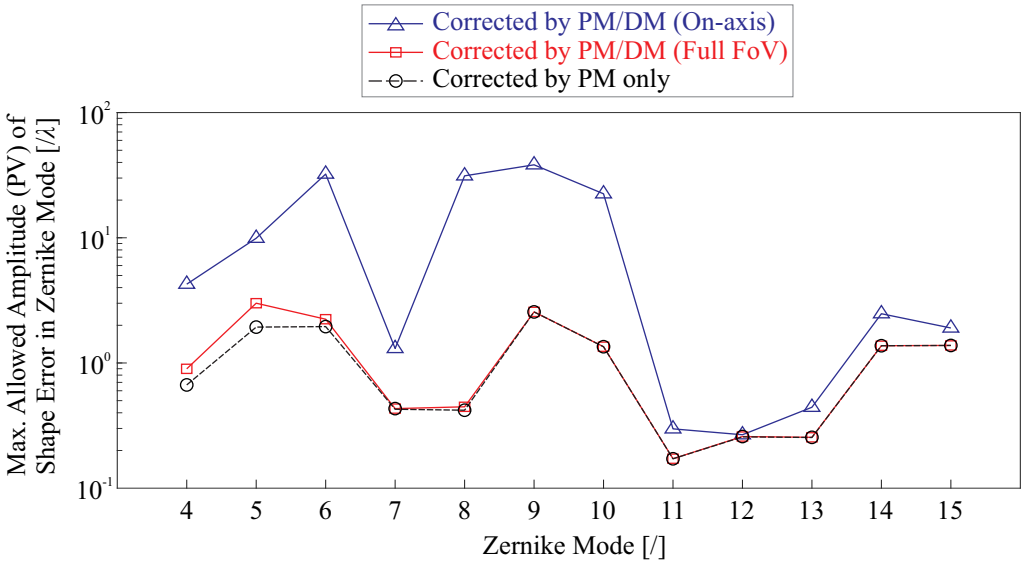

Figure 15. Maximum allowed amplitudes of surface errors (in λ) for different modes.

5. Conclusions

This paper discusses the wavefront control strategies for a large active thin-shell primary mirror with unimorph actuators. The lightweight thin shell with a doubly curvature is covered by an active layer (piezoelectric or electrostrictive) and the deformation is made by the strain actuation. The curvature-induced rigidity of the thin-shell structure deteriorates the performances of the forming accuracy of the active reflector and the morphing stroke of the actuators, relating to a structural parameter of $\sqrt{R_C t}$. The structure can be softened by a petal-like division of the mirror surface, exhibiting a much larger morphing amplitude with a constant voltage consumption; however, this may lead to larger responses (shape errors) excited by the environmental disturbances. The performances of the forming accuracy are

also compared, between the petal-like segmented and monolithic configurations of the reflectors, showing a modal dependency on the capacities of the optical error reduction. The performances of correcting the wavefront errors can be further enhanced by using other active surfaces in the optical chain; a numerical example of an R-C telescope is tested, where the unimorph thin-shell reflector acts as the primary mirror, and a deformable relay mirror is supplemented to compensate the residual wavefront errors. An augmentation can be achieved on the error budget of the shape error for the addition of the complementary correction by the relay mirror, especially for an on-axis observation in space with complex environmental disturbances.

Author Contributions: Conceptualization, K.W. and A.P.; methodology, K.W. and A.P.; software, K.W. and Y.Y.; validation, K.W., Y.Y. and A.P.; writing—original draft preparation, K.W.; writing—review and editing, K.W. and A.P.; All authors have read and agreed to the published version of the manuscript.

Funding: The research is supported by the National Natural Science Foundation of China (62105249), the Open Fund of Hubei Luojia Laboratory (220100052), the Fundamental Research Funds for the Central Universities (2042022kf1065), and the Natural Science Foundation of Hubei Province (2022CFB664). The part conducted at ULB is supported by ESA-ESTEC in the framework of the GSTP program, project Multilayer Adaptive Thin Shell Reflectors for Future Space Telescopes (MATS).

Institutional Review Board Statement: Not applicable.

Informed Consent Statement: Not applicable.

Data Availability Statement: Not applicable.

Acknowledgments: The authors wish to thank G. Rodrigues and D. Alaluf from ESA-ESTEC for their contributions to the earlier stages of this project.

Conflicts of Interest: The authors declare no conflicts of interest.

Abbreviations

The following abbreviations are used in this manuscript:

AMTD	Advanced Mirror Technology Development
AMSD	Advanced Mirror System Demonstrator
BLAST	Balloon-borne Large Aperture Submillimeter Telescope
CTE	Coefficient of Thermal Expansion
ELT	Extremely Large Telescopes
ESA	European Space Agency
FoV	Field of View
HST	Hubble Space Telescope
JWST	James Webb Space Telescope
LIS	Large Inflatable Structures
LRD	Inflatable Reflector Development
LS	Least Squares
MISSE	Materials International Space Station Experiment
MMSD	Multiple Mirror System Demonstrator
NASA	National Aeronautics and Space Administration
PET	PolyEthylene Terephthalate
PI	PolyImide
PV	Peak to Valley
PVDF-TrFE	PolyVinyliDene Fluoride-co-TriFluoroEthylene
RMS	Root Mean Square
R-C	Ritchey–Chrétien
SE-L2	Sun–Earth Lagrange point 2

SiC	Silicon Carbide
ULB	Université Libre de Bruxelles
ULE	Ultra-Low Expansion glass

Appendix A

The Zernike mode $Z_i(\rho, \theta)$ is defined on a unit circle in polar coordinates (ρ, θ) where $0 < \rho < 1$, and it is usually used as a modal basis to describe the wavefront w on the pupil. Table A1 gives a list of analytical expressions of Zernike modes with an order of $i = 1 - 21$ in Noll's index [27], with a normalization of

$$\int_0^{2\pi} \int_0^1 Z_i^2 \rho d\rho d\theta = \pi \tag{A1}$$

Table A1. Analytical expressions of the low-order Zernike modes (in Noll's index).

Term	Analytical Expression	Classical Name
Z1	1	Piston
Z2	$2\rho\cos\theta$	Horizontal Tilt
Z3	$2\rho\sin\theta$	Vertical Tilt
Z4	$\sqrt{3}(2\rho^2 - 1)$	Defocus
Z5	$\sqrt{6}\rho^2\sin 2\theta$	Oblique Astigmatism
Z6	$\sqrt{6}\rho^2\cos 2\theta$	Vertical Astigmatism
Z7	$\sqrt{8}(3\rho^3 - 2\rho)\sin\theta$	Vertical Coma
Z8	$\sqrt{8}(3\rho^3 - 2\rho)\cos\theta$	Horizontal Coma
Z9	$\sqrt{8}\rho^3\sin 3\theta$	Vertical Trefoil
Z10	$\sqrt{8}\rho^3\cos 3\theta$	Oblique Trefoil
Z11	$\sqrt{5}(6\rho^4 - 6\rho^2 + 1)$	Primary Spherical Aberration
Z12	$\sqrt{10}(4\rho^4 - 3\rho^2)\cos 2\theta$	Vertical Secondary Astigmatism
Z13	$\sqrt{10}(4\rho^4 - 3\rho^2)\sin 2\theta$	Oblique Secondary Astigmatism
Z14	$\sqrt{10}\rho^4\cos 4\theta$	Vertical Quadrafoil
Z15	$\sqrt{10}\rho^4\sin 4\theta$	Oblique Quadrafoil
Z16	$\sqrt{12}(10\rho^5 - 12\rho^3 + 3\rho)\cos\theta$	N/A
Z17	$\sqrt{12}(10\rho^5 - 12\rho^3 + 3\rho)\sin\theta$	N/A
Z18	$\sqrt{12}(5\rho^5 - 4\rho^3)\cos 3\theta$	N/A
Z19	$\sqrt{12}(5\rho^5 - 4\rho^3)\sin 3\theta$	N/A
Z20	$\sqrt{12}\rho^5\cos 5\theta$	N/A
Z21	$\sqrt{12}\rho^5\cos 5\theta$	N/A

References

1. Fanson, J.; Bernstein, R.; Angeli, G.; Ashby, D.; Bigelow, B.; Brossus, G.; Bouchez, A.; Burgett, W.; Contos, A.; Demers, R.; et al. Overview and Status of the Giant Magellan Telescope Project. In Proceedings of the SPIE Astronomical Telescopes + Instrumentation, Online, 14–18 December 2020; p. 114451F.
2. Tamai, R.; Koehler, B.; Cirasuolo, M.; Biancat-Marchet, F.; Tuti, M.; Herrera, J.C.G.; Ramsay, S. Status of the ESO's ELT Construction. In Proceedings of the SPIE Astronomical Telescopes + Instrumentation, Montréal, ON, Canada, 17–22 July 2022; p. 121821A.
3. Wang, K. Piezoelectric Adaptive Mirrors for Ground-based and Space Telescopes. Ph.D. Thesis, Université Libre de Bruxelles, Brussels, Belgium, 2019.
4. Palisoc, A.; Veal, G.; Cassapakis, C.; Greschik, G.; Mikulas, M.; Geometry Attained by Pressurized Membranes. In Proceedings of the SPIE Astronomical Telescopes + Instrumentation, Kona, HI, USA, 3–5 March 1998; p. 335611.
5. Chodimella, S.; Moore, J.; Otto, J.; Fang, H. Design Evaluation of a Large Aperture Deployable Antenna. In Proceedings of the 47th AIAA/ASME/ASCE/AHS/ASC Structures, Structural Dynamics, and Materials Conference, Newport, RI, USA, 1–4 May 2006; p. 1603.
6. Flint, E.; Bales, G.; Glaese, R.; Bradford, R. Experimentally Characterizing the Dynamics of 0.5 m Diameter Doubly Curved Shells Made from Thin Films. In Proceedings of the 44th AIAA/ASME/ASCE/AHS/ASC Structures, Structural Dynamics, and Materials Conference, Norfolk, VA, USA, 7–10 April 2003; pp 1831.
7. Freeland, R.; Bilyeu, G. In-step Inflatable Antenna Experiment. *J. Acta Astronaut.* **1993**, *30*, 29-–40. [CrossRef]

8. Flint, E.; lindler, J.; Hall, J.; Rankine, C.; Regelbrugge, M. Overview of Form Stiffened Thin Film Shell Characteristic Behavior. In Proceedings of the 47th AIAA/ASME/ASCE/AHS/ASC Structures, Structural Dynamics, and Materials Conference, Newport, RI, USA, 1–4 May 2006; p. 1900.
9. Keller, P.; Lake, M.; Codell, D.; Barrett, R.; Taylor, R.; Schultz, M. Development of Elastic Memory Composite Stiffeners for a Flexible Precision Reflector. In Proceedings of the 47th AIAA/ASME/ASCE/AHS/ASC Structures, Structural Dynamics, and Materials Conference, Newport, RI, USA, 1–4 May 2006; p. 2179.
10. Morgan, R.M.; Agnes, G.A.; Barber, D.; Dooley, J.; Dragovan, M.; Hatheway, A.E.; Marcin, M. The DART Cylindrical Infrared 1-meter Membrane Reflector. In Proceedings of the SPIE Optical Fabrication, Metrology, and Material Advancements for Telescopes, Glasgow, UK, 24 September 2004; p. 549412.
11. Degroh, K.K.; Jaworske, D.A.; Pippin, G.; Jenkins, P.P.; Walters, R.J.; Thibeault, S.A.; Palusinski, I.; Lorentzen, J.R. Materials International Space Station Experiment (MISSE): Overview, Accomplishments and Future Needs. In *Annual International Space Station Research and Development Conference*; GRC-E-DAA-TN15048; NASA: Washington, DC, USA, 2014.
12. Palisoc, A.L.; Veal, G. Large Telescope Using a Holographically-corrected Membrane Mirror. In *Technical Report to NASA Institute for Advanced Concepts*; LTR-00-AP-021; NASA: Washington, DC, USA, 2000;
13. Stahl, H.P. Lightweight Optics: Optical to IR. In *NASA Astrophysics Subcommittee Meeting*; MSFC-E-DAA-TN30485; NASA: Washington, DC, USA, 2016
14. Bastaits, R.; Rodrigues, G.; Jetteur, P.H.; Hagedorn, P.; Preumont, A. Multi-layer Adaptive Thin Shells for Future Space Telescopes. *Smart Mater. Struct.* **2012**, *21*, 064004. [CrossRef]
15. Wang, K.; Godfroid, T.; Robert, D.; Preumont, A. Electrostrictive PVDF-TrFE Thin Film Actuators for the Control of Adaptive Thin Shell Reflectors. *Actuators* **2020**, *9*, 53. [CrossRef]
16. Wang, K.; Godfroid, T.; Robert, D.; Preumont, A. Adaptive Shell Spherical Reflector Actuated with PVDF-TrFE Thin Film Strain Actuators. *Actuators* **2021**, *10*, 7. [CrossRef]
17. Vreedenburgh, C.G.J. The Shell with Double Curvature Considered as a Plate on an Elastic Foundation. *HERON* **1962**, *10*, 2–19.
18. Preumont, A. *Vibration Control of Active Structures, an Introduction*, 4th ed.; Springer: Cham, Switzerland, 2018.
19. Wang, K.; Alaluf, D.; Rodrigues, G.; Preumont, A. Precision Shape Control of Ultra Thin Shells with Strain Actuators. *J. Appl. Comput. Mech.* **2021**, *7*, 1130–1137.
20. Uchino, K. Electrothermal Phenomena in Ferroelectrics. *Actuators* **2020**, *9*, 93. [CrossRef]
21. Nielsen, C.J.G.; Tian, D.; Wang, K.; Preumont, A. Adaptive Deployable Thin Spherical Shell Reflectors. *Actuators* **2022**, *11*, 198. [CrossRef]
22. Schroeder, D.J. *Astronomical Optics*, 2nd ed.; Academic Press: Cambridge, MA, USA, 2000.
23. Bastaits, R. Extremely Large Segmented Mirrors: Dynamics, Control and Scale Effects. Ph.D. Thesis, Université Libre de Bruxelles, Brussels, Belgium, 2010.
24. Soedel, W. A Natural Frequency Analogy between Spherically Curved Panels and Flat Plates. *J. Sound Vib.* **1973**, *29*, 457–461. [CrossRef]
25. Wang, K.; Preumont, A. Shape Control of an Adaptive Spherical Shell Reflector under Space Environment. In Proceedings of the 8th Symposium on Novel Photoelectronic Detection Technology and Applications, Kunming, China, 9–11 November 2021; p. 12169A5.
26. Madec, P.Y. Overview of Deformable Mirror Technologies for Adaptive Optics and Astronomy. In Proceedings of the SPIE Astronomical Telescopes + Instrumentation, Amsterdam, The Netherlands, 13 September 2012; p. 844705.
27. Noll, R.J. Zernike Polynomials and Atmospheric Turbulence. *JOSA* **1976**, *66*, 207–211. [CrossRef]